Atmos. Meas. Tech. Discuss., doi:10.5194/amt-2016-59, 2016
Manuscript under review for journal Atmos. Meas. Tech.
Published: 18 April 2016

Open-loop GPS signal tracking at low elevation angles from a ground-based observation site

Georg Beyerle and Florian Zus

GFZ German Research Centre for Geosciences, Potsdam, Germany

Correspondence to: Georg Beyerle, GFZ German Research Centre for Geosciences, Telegrafenberg, D-14473 Potsdam, Germany (gbeyerle@gfz-potsdam.de)

Abstract. A one-year data set of ground-based GPS signal observations aiming at geometric elevation angles below $+2°$ is analyzed. Within the "GLESER" measurement campaign about 2600 validated setting events were recorded by the "OpenGPS" open-loop tracking receiver at an observation site located at 52.3808°N, 13.0642°E between January and December 2014. The measurements confirm the feasibility of open-loop signal tracking down to geometric elevation angles of $-1°$ to $-1.5°$ extending the corresponding closed-loop tracking range by up to 1°. The study is based on the premise that observations of low-elevation events by a ground-based receiver may serve as test cases for space-based radio occultation measurements, even if the latter proceed at a significantly faster temporal scale. The results support the conclusion that the open-loop Doppler model has negligible influence on the derived carrier frequency profile for strong signal-to-noise density ratios above about 30 dB Hz. At lower signal levels, however, the "OpenGPS" receiver's dual-channel design, which tracks the same signal using two Doppler models with a 10 Hz offset, uncovers a notable bias. The repeat patterns of the GPS orbit traces in terms of azimuth angle reveal characteristic signatures in both, signal amplitude and Doppler frequency with respect to the topography close to the observation site. On the other hand, vertical refractivity gradients extracted from ECMWF meteorological fields correlate moderately well with observed signal amplitude fluctuations at negative geometric elevation angles emphasizing the information content of low-elevation GPS signals with respect to the atmospheric state within the planetary boundary layer.

1 Introduction

For more than a decade space-based Global Navigation Satellite System (GNSS) radio occultation (GNSS-RO) has established itself as a valuable measurement technique for atmospheric remote sensing. Vertical profiles of ray bending angle, refractivity, dry pressure and temperature are used by several meteorological centres for assimilation into numerical weather prediction models (see, e.g., Cucurull et al., 2007; Anthes et al., 2008; Healy and Thepaut, 2006; Liu and Xue, 2014; Poli et al., 2010; Rennie, 2010, and references therein). Moreover, climate studies increasingly take advantage of validated GNSS-RO data sets (see, e.g., Foelsche et al., 2011; Ringer and Healy, 2008; Steiner et al., 2011; Gleisner and Healy, 2013; Schmidt et al., 2010; Poli et al., 2010, and references therein).

A number of past and current spacecrafts carry GNSS-RO payloads, e.g. the satellites GPS/Met (Kursinski et al., 1997), CHAMP (Wickert et al., 2001), GRACE (Beyerle et al., 2005; Wickert et al., 2005), COSMIC (Anthes et al., 2008), Metop

(Luntama et al., 2008; von Engeln et al., 2011; Bonnedal et al., 2010; Zus et al., 2011), TerraSAR-X (Beyerle et al., 2011), TanDEM-X (Zus et al., 2014). Already the proof-of-concept mission GPS/Met revealed the difficulties of retrieving dual frequency carrier phase data when the ray tangent point enters the lower troposphere (Rocken et al., 1997). More specifically, Rocken et al. (1997) noticed a significant negative refractivity bias in the lower troposphere at tropical latitudes. At low altitudes the GNSS signals experience multipath beam propagation (see, e.g., Gorbunov, 2002; Hocke et al., 1999). The resulting optical path length differences lead to constructive and destructive interferences and the corresponding signal amplitude fluctuations increase the probability of an early loss of tracking lock.

To address these issues new signal tracking methods were developed and implemented. Whereas the "fly-wheeling" tracking method of JPL's "Blackjack" GPS receivers mounted on CHAMP and GRACE (Hajj et al., 2004), showed some progress, significant improvements with respect to probing of the planetary boundary layer, in particular at low latitudes, were obtained with the introduction and implementation of open-loop (O/L) tracking (or raw-sampling) techniques (see, e.g., Sokolovskiy, 2001; Sokolovskiy et al., 2006; Ao et al., 2009; Bonnedal et al., 2010).

The open-loop signal tracking mode successfully resolves the problem of premature loss of signal in the lower troposphere at low latitudes (Sokolovskiy, 2001; Sokolovskiy et al., 2006). In contrast to closed-loop (C/L) tracking, a receiver operating in open-loop mode partially or completely disregards the tracking loop feedback values from the carrier and code discriminators, but instead steers the corresponding numerically-controlled oscillators (NCOs) using a-priori parameters. In the following these O/L parameters, which are usually derived from an atmospheric climatology, are referred to as "O/L model". The time duration, which the receiver operates in open-loop tracking mode, may be controlled by predetermined threshold values in terms of tangent point altitude, elevation angle and/or signal-to-noise ratio (SNR). While these general considerations apply to all open-loop / raw-sampling implementations, the specific realizations vary in detail (see, e.g., U.S. patents US6731906 B2 and US6720916 B2).

A key requirement for the adoption of O/L signal tracking in operational GNSS-RO missions is the insensitivity of derived carrier phase paths and code pseudoranges on the particular choice of O/L model. According to Sokolovskiy (2001) the requirement is met, provided the true atmospheric Doppler profile deviates by not more than half of the sampling frequency from the O/L Doppler model. With a typical sampling rate of $f_s = 50$ Hz this requirement translates into a maximum frequency deviation of 25 Hz.

Recently, Beyerle et al. (2011) claimed on the basis of GNSS-RO observations recorded by the "IGOR" receiver aboard the TerraSAR-X spacecraft, that the O/L Doppler model may influence the derived refractivity values for low signal amplitudes below about 25 V/V and potentially contribute to the negative refractivity bias. In order to substantiate this hypothesis they proposed to track each GNSS-RO signal with two O/L models, separated in frequency space by a predefined offset. We note, however, that other causes certainly contribute to the observed refractivity bias as well (see, e.g., Gorbunov et al., 2015; Sokolovskiy et al., 2010, and references therein). Since "IGOR" firmware modification aboard TerraSAR are unfeasible, two indirect methods were investigated. First, a measurement campaign was conducted in late 2012 with the GNSS-RO receivers aboard the TerraSAR-X and TanDEM-X satellites recording signals from the same setting GPS satellites, but using different O/L models (F. Zus et al. (2014), "GPS radio occultation with TerraSAR-X and TanDEM-X: sensitivity of lower troposphere sounding to the Open-Loop Doppler model", Atmos. Meas. Tech. Discuss., 7, 12719–12733, doi:10.5194/amtd-7-12719-2014, unpublished). Second, within the framework of the "GLESER" (GPS low-elevation setting event recorder) measurement campaign a ground-based experiment was devised and established at an observation site on the "Albert Einstein" science campus in Potsdam, Germany (52.3808°N, 13.0642°E) in December 2010. The "GLESER" campaign targets signals from GPS satellites at low elevations as they set beyond the horizon at elevation angles below $+2°$. The measurement hardware, a single-frequency "OpenGPS" receiver, is an in-house development based on C. Kelley's "OpenSourceGPS" concept (Kelley, 2002).

Whilst ground-based observations of low-elevation setting events do not allow to derive bending angle profiles for ray tangent points above the receiver altitude (Zuffada et al., 1999; Haase et al., 2014; Healy, 2002; Sokolovskiy et al., 2001), these measurements nevertheless are useful to investigate receiver tracking behaviour under multipath conditions with strongly fluctuating SNRs. In addition, the signal excess phase paths have been shown to be sensitive to the local refractivity field (see, e.g., Lowry et al., 2002; Zus et al., 2015). During a typical low-elevation setting event the geometric elevation angle, i.e. the ray's elevation angle at the receiver antenna, disregarding atmospheric refraction effects, decreases from $+2°$ at the measurement start to about $-1°$ to $-1.5°$ at the end of the observation. Setting events last for about 10 to 15 minutes on average; hence their durations are about an order of magnitude longer than typical space-based radio occultation measurements (see, e.g. Kursinski et al., 1997). Even if a ground-based observation does not lend itself to the derivation of bending angle profiles (Zuffada et al., 1999; Haase et al., 2014; Healy, 2002; Sokolovskiy et al., 2001), from the signal tracking perspective we may still regard "GLESER" recordings as radio occultation events in slow motion. The present study is restricted to the observation and analysis of setting events; an extension towards rising events, however, is feasible from a technical standpoint and may be considered in the future.

The paper is sectioned as follows. First, GFZ's "OpenGPS" instrument, which has participated in several ground-based and airborne measurement campaigns during the last decade, is described. Closed-loop and open-loop tracking methods are briefly reviewed and the receiver's capabilities are illustrated with some example profiles. The section ends with a cursory review of the "OpenGPS" hardware and software. Second, the measurements conducted during the "GLESER" campaign are introduced and the data processing algorithms and analysis methods are discussed. In the final and main section of this paper the measurement results are discussed and put into perspective.

2 Instrument description

The "GLESER" campaign utilizes the "OpenGPS" instrument, a single-frequency 12 channel GPS receiver. Several copies of this device, which is based on C. Kelley's "OpenSourceGPS" concept (Kelley, 2002), were built at GFZ and used in various ground-based and airborne GPS measurement campaigns (see, e.g., Helm, 2008, and Helm et al., 2004, "Detection of coherent reflections with GPS bipath interferometry", unpublished, preprint available at http://arxiv.org/abs/physics/0407091). In order to provide a self-consistent description of the "OpenGPS" instrument and its O/L signal tracking implementation, we begin with a brief review of C/L and O/L tracking techniques.

Atmos. Meas. Tech. Discuss., doi:10.5194/amt-2016-59, 2016
Manuscript under review for journal Atmos. Meas. Tech.
Published: 18 April 2016

2.1 Closed-loop and Open-loop Signal Tracking

It well known that inhomogeneities in the tropospheric water vapour field, in particular at low latitudes, can produce multipath propagation of GNSS signals at low elevation angles (see, e.g., Gorbunov et al., 2004; Beyerle et al., 2003). Space-based RO observations show that under these conditions SNR values exhibit strong fluctuations, which early GNSS-RO receivers were unable to track properly (Rocken et al., 1997). To address premature signal loss GNSS-RO receiver tracking algorithms based on closed feed-back loops were replaced by "open-loop" techniques (see, e.g., Sokolovskiy, 2001; Sokolovskiy et al., 2006; Ao et al., 2009; Bonnedal et al., 2010). If a receiver operates in open-loop mode the feed-back loop is opened and the NCO producing the replica signal is steered (in part or fully) from model parameters. This model takes into account the expected signal dynamics from both, the transmitter and receiver orbits, clocks biases and drifts as well as the signal propagation characteristics in the lower troposphere. The latter are typically obtained from an atmospheric climatology (Sokolovskiy, 2001; Bonnedal et al., 2010).

The schematic in fig. 1 illustrates the two tracking concepts for carrier phase tracking; corresponding considerations apply to code tracking as well. In standard C/L tracking (fig. 1, top panel) the down-converted input signal ("input") is correlated with two internal replica signals ("sin" and "cos") generated by the NCO (see, e.g., Misra and Enge, 2006). The result is low-pass filtered (represented by the box labeled "average"), the carrier phase discriminator determines phase deviations between the observed and modeled replica and provides appropriate adjustments to the loop filter. The "sin" and "cos" replica signals, the latter being phase shifted by a quarter cycle, i.e. 90° with respect to the former, allow to distinguish phase advances from phase delays between observed and replica signal. The phase discriminator output is digitally filtered ("loop filter") to prevent unstable loop behaviour (see, e.g., Lindsey and Chie, 1981; Thomas, 1989). The receiver output samples ("carrier phase output") combine the NCO model phases and the phase residuals from the discriminator to yield the observed carrier phase.

If signal amplitudes drop below certain threshold levels, the corresponding phase residuals start to be dominated by noise and proper alignment between replica and observed signal can no longer be maintained. Fig. 2 shows exemplarily the signal-to-noise density ratio C/N_0 (Badke, 2009; Kaplan, 1996; Parkinson and Spilker, 1996) as a function of geometric elevation angle for a setting event recorded in the morning of 1 January 2015. At elevation angles below about $+1.5°$ the density ratios C/N_0 start to fluctuate. At about $+1.19°$ and again at $+0.56°$ transient signal gaps with $C/N_0 \lesssim 30$ dB Hz occur which last for less than about 0.5 s. During these time intervals the phase discriminator output is dominated by noise causing enhanced NCO Doppler frequency fluctuations as is illustrated in fig. 3 (blue line). At about $-0.26°$ elevation low signal level conditions persist for a longer time period and the carrier NCO frequency deviates by hundreds of Hz (blue line in fig. 3). Correspondingly, C/N_0 drops by about 20 dB down to the noise level (fig. 2) and never recovers during the last part of this setting event.

Open-loop tracking is immune to transient SNR gaps, even if these breaks stretch across extended time periods. The bottom panel of fig. 1 schematically illustrates the concept. In O/L tracking mode the feedback loop is removed and the NCO is solely controlled by model values. The correlation output values, produced by the "cos" and "sin" branches, are denoted by "in-phase" and "quad-phase" correlation samples, respectively (Sokolovskiy, 2001; Sokolovskiy et al., 2006; Ao et al., 2009;

Atmos. Meas. Tech. Discuss., doi:10.5194/amt-2016-59, 2016
Manuscript under review for journal Atmos. Meas. Tech.
Published: 18 April 2016

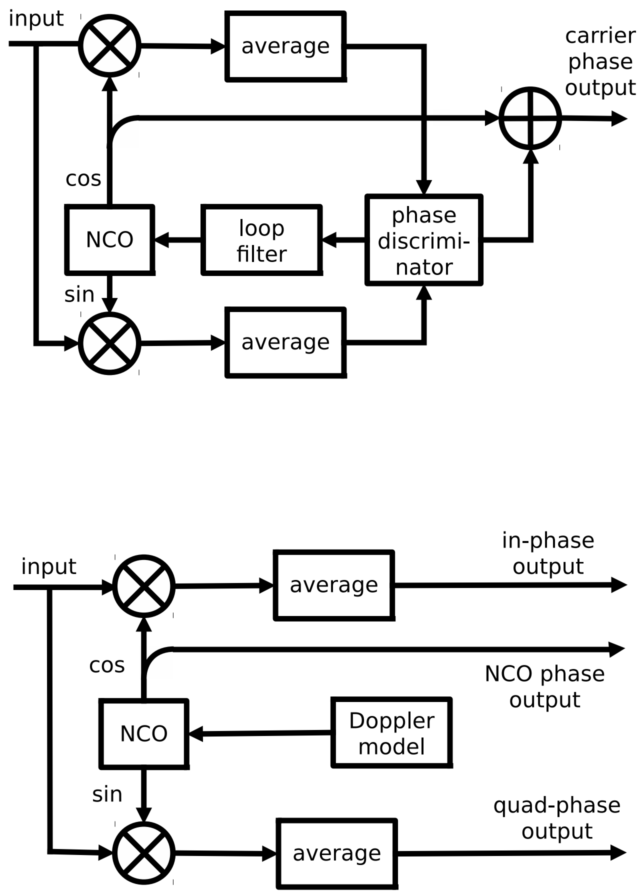

Figure 1. Schematic representation of closed-loop (top panel) and open-loop (bottom) carrier signal tracking. In closed-loop mode the "input" signal is correlated with two replica signals, "sin" and "cos", the latter is phase-shifted by 90° with respect to the former. The correlation sums are low-pass filtered and the output is examined for phase deviations between input and replica signal. The discriminator adjustments close the feedback loop. Open-loop tracking (bottom panel) dispenses with the phase discriminator and the numerically controlled oscillator ("NCO") is solely steered from model values ("Doppler model"). The observed carrier phase finally is assembled from the NCO phases and the in-phase and quad-phase correlation samples.

Bonnedal et al., 2010). In low-SNR conditions the in-phase and quad-phase samples are dominated by noise. However, since no feedback is present in O/L tracking, these noisy samples cannot produce erroneous control input to the NCO and transient signal gaps do not cause loss of tracking lock as illustrated in figs. 2 and 3. Red and green lines show C/N_0 (fig. 2) and the NCO carrier frequency (fig. 3) recorded by the receiver's two open-loop channels, respectively. In the following the two channels are denoted by the letters A and B. Both channels are attached to the same PRN and therefore track the same transmitter. Their corresponding NCO frequencies are derived from the same model, but on channel A's value an additional -5 Hz, on B an additional $+5$ Hz is added, resulting in a 10 Hz inter-channel offset. This 10 Hz shift can clearly be identified in fig. 3 (insert);

Atmos. Meas. Tech. Discuss., doi:10.5194/amt-2016-59, 2016
Manuscript under review for journal Atmos. Meas. Tech.
Published: 18 April 2016

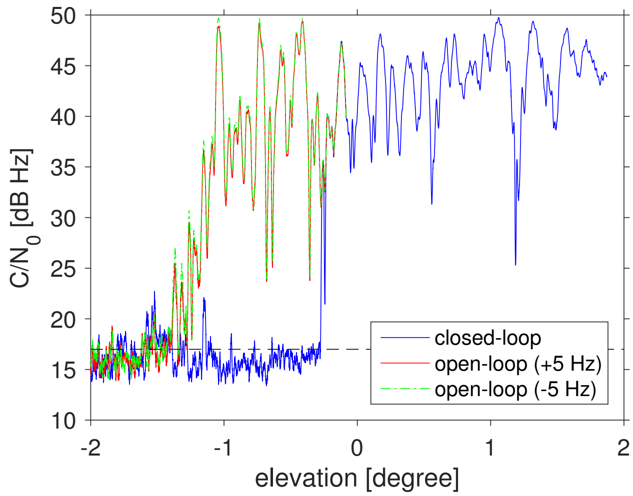

Figure 2. Observed signal-to-noise density ratio C/N_0 as a function of geometric satellite elevation angle. Atmospheric bending amounts to about $1°$ to $2°$ at the observation site and therefore the two open-loop channels (green and red) continue to track the signal down to elevation angles of about $-1.2°$. A strong amplitude fluctuation at about $-0.26°$ causes the closed-loop channel (blue) to lose tracking lock much earlier than the open-loop channels (green and red). The noise level of about 17 dB Hz is marked in black. Constructive interference produce high C/N_0 values exceeding 48 dB Hz at elevations below $-1°$. This observation of GPS PRN 7 was recorded on 1 January 2015 between 6:38 h and 6:52 h GPS time.

here, O/L tracking mode starts at an elevation angle of $-0.08°$ and reaches the nominal 10 Hz shift after a short settling phase at $-0.13°$ elevation.

2.2 OpenGPS receiver hardware

The "OpenGPS" instrument, a photograph of the PCI card is reproduced in fig. 4, inherited its key design features from the "OpenSourceGPS" project (Kelley, 2002). It utilizes the NovAtel® "Superstar 1" (formerly CMC Electronics®) GPS module (outlined red in fig. 4) and is based on the well-documented Zarlink® (formerly Mitel Semiconductor®) GPS chip set consisting of the single-frequency front-end GP2015 and the hardware correlator GP2021 (Zarlink, 2005).

During signal acquisition and tracking the 12 detection channels of the GP2021 hardware correlator provide in-phase and quad-phase correlations sums at the end of each full C/A code sequence. The occurrences are denoted "DUMP" events and repeat at a rate of about once every millisecond (Zarlink, 2005). "DUMP" events are aligned to the individual C/A code sequences and therefore are asynchronous events. A real-time operating system (Linux OpenSUSE version 11.3 with RTAI (RealTime Application Interface for Linux) version 3.8.1 kernel extension module) ensures that the correlator registers are read and processed within these time constraints.

Atmos. Meas. Tech. Discuss., doi:10.5194/amt-2016-59, 2016
Manuscript under review for journal Atmos. Meas. Tech.
Published: 18 April 2016

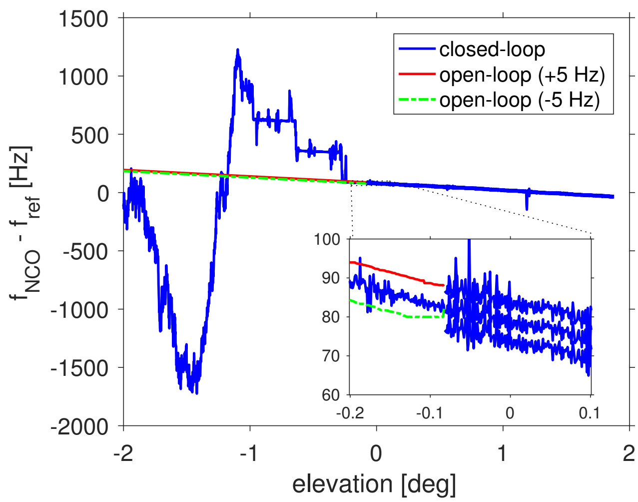

Figure 3. Carrier NCO frequency as a function of geometric satellite elevation angle. For clarity, a constant frequency value of $f_{\mathrm{ref}} = 1.4071$ MHz is subtracted. The transition between closed-loop and open-loop tracking is depicted in the insert highlighting the 10 Hz offset between the two O/L channels. Same event as shown in fig. 2.

In addition, the current values of the carrier and code NCOs are output as well. In contrast to "DUMP"'s, these "TIC" events occur simultaneously on all active channels and can be triggered at a used-defined frequency. Linux RTAI meets the necessary time constraints for correlator input and output with latency times below about 3–5 μs as measured on the "OpenGPS" hardware.

The "OpenGPS" hardware utilizes a modified "Superstar 1" circuit board. Following the "OpenSourceGPS" concept (Kelley, 2002) the on-board processing unit ARM7TDMI and memory chip are unsoldered from the board and the modified module is mounted on a PROTO-3 (manufactured by KOLTER ELECTRONIC®) prototyping board which plugs into a PCI expansion slot of a standard PC.

The signal acquisition and tracking program runs on the host computer; control, monitoring and readout of the GP2021 hardware correlator is performed through the PROTO-3's PCI port. An interface module, which was designed and built in-house using discrete TTL logic (outlined blue in fig. 4), connects to the hardware correlator's input and output registers and allows direct access to the correlator registers from the host PC via the PCI interface bus.

Compared to conventional GPS receivers with on-board processing units the "OpenGPS" design clearly has some disadvantages. Using a PCI expansion card for signal front-end as well as down-conversion and performing signal acquisition and tracking on a host PC implies larger size, mass and power consumption. On the other hand, the CPU processing power of the host PC surpasses the capabilities of the "Superstar 1" onboard processor by a wide margin. The "OpenGPS" instrument therefore allows to operate the hardware correlator at higher sampling rates, to extract additional data from the correlation pro-

Atmos. Meas. Tech. Discuss., doi:10.5194/amt-2016-59, 2016
Manuscript under review for journal Atmos. Meas. Tech.
Published: 18 April 2016

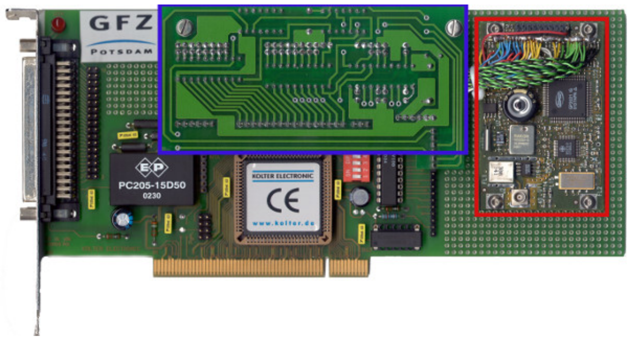

Figure 4. GFZ's "OpenGPS" receiver board for PCI interface bus. A PCI prototyping board carries a modified single-frequency GPS module (red outline). Data cables connect the input/output ports of the hardware correlator chip to the TTL logic board (blue) and the PCI interface.

cess (e.g., in-phase and quad-phase correlation samples from both GP2021 delay branches) and to run a full-featured operating system with network layer and graphical display capabilities in addition to the real-time process.

During the "GLESER" measurement campaign a mini-PC (Shuttle® XPC SB52G2) equipped with 760 MByte memory and an Intel Pentium 4 processor clocked at 1.8 GHz serves as host PC. Despite this by today's standards modest hardware the instrument supports sampling frequencies of up to 100 Hz; the observations described and discussed in the following are recorded at 50 Hz.

2.3 OpenGPS receiver software

The "OpenGPS" signal acquisition, tracking and real-time processing software originates from the "OpenSourceGPS" project as well (Kelley, 2002); it also draws from source code written by S. Esterhuizen and van Leeuwen (2002). The main tasks of the receiver program are

- search and acquisition in code and frequency space,
- signal tracking using code delay and carrier phase-locked loops,
- decoding of the navigation data modulation,
- calculation of transmitter position and velocity from broadcast ephemeris,
- calculation of receiver position and receiver clock bias from measured pseudoranges,
- output of raw data to disk

(see, e.g., Misra and Enge, 2006; Tsui, 2000). Since the timeliness requirements for these tasks differ by several orders of magnitude these tasks are allocated to two processes running in parallel, the kernel module `ogrcvr_mod.ko` and the user space application `ogrcvr`. The module `ogrcvr_mod.ko` executes tasks controlling the code and carrier phase tracking

```
OpenGPS v0.7.3 (Nov 16 2012 12:10:09)  time: 1866/484891  Fri Oct 16 14:41:39 2015
(init) lat:  52.37920 deg  lon:   13.06630 deg  hae: 144.00 m  rfl.hght:    0.0 m
(obs)  lat:  52.38079 deg  lon:   13.06409 deg  hae: 168.00 m  clk bias: 143045.34 us
(avg)  lat:  52.38083 deg  lon:   13.06421 deg  hae: 162.78 m  clk drift:  2438.58 ns/s
(obs) north:   0.00 m/s  east:   0.00 m/s  vert:   0.00 m/s
GDOP:  5.7  HDOP:  2.2  VDOP:  3.9  acc_new: 000  acc_miss: 4000  acq: 625
nav:  6 !nav:  2  almanac rec'd: 31  # masters: 1 (max) # clones: (fr=0/sl=0,max=2)
cold PRN: 29  TIC frq:  50 Hz, CPU:   5.6(377.5) us  log: nav=0/obs=1/trk=0
trk: >-2 deg elev, nav: >10 deg elev, rec: [-160,-20] deg azim, [-2,2] deg elev, o/l: 0 deg
nav: nav-1866-484832.dat, trk: trk-1866-484832.dat
# Tic: 134907622, # NavFix: 134907622
--- page 0 ---
ch prn fe st    azim   elev dir  CN0  lock sync   frq frqadjust  frm sfd val page mis parity
  1 28 0 Pn2   -98.15   1.64 -  41.9  1.00 (1/1)    0 (  75/ -5) 213  1  7 52/13    1 1063/1
  2  1 0 Pn2   155.50  77.78 -  44.7  1.00 (1/1)    1 (-164/  2) 333  1  7 52/13    1 1612/18
  3 32 0 Pn2    72.88  71.19 -  36.8  1.00 (1/1)    1 (-386/ -6) 341  1  7 52/13    1 1594/28
  4 11 0 Pn2   175.02  56.91 -  45.1  1.00 (1/1)    0 ( 221/  5) 451  1  7 52/13    1 2153/17
  5 17 0 Pn2   -56.08  34.05 +  44.2  1.00 (1/1)    0 ( -12/  1)  31  1  7 52/13    1 151/0
  6 10 0 aq      0.00   0.00     0.0  0.00 (0/0)   22 (   0/  0)   0  0  7  0/ 0    1 0/0
  7 19 0 Pn2  -154.47  37.45 -  45.7  1.00 (1/1)    2 (  19/  4) 411  1  7 52/13    1 2052/1
  8  3 0 Pn2   -99.13  66.03 +  46.2  1.00 (1/1)    1 (  56/ -1) 174  1  7 52/13    1 818/18
  9  4 0 aq    134.95  47.63 -   0.0  0.00 (0/0)  -10 (   0/  0)   0  0  7  0/ 0    1 0/0
 10  8 0 Pn2   179.88   5.09 -  35.8  1.00 (1/1)    2 (-252/  9) 670  1  7 52/13    1 3237/29
 11 28 0 oc o  -98.15   1.64 -  25.9 -0.01 (0/0)    0 (  75/ -5)   0  0  7  0/ 0    1 0/0
 12 28 0 oc o  -98.15   1.64 -  26.1  0.01 (0/0)    0 (  75/ -5)   0  0  7  0/ 0    1 0/0

  ch (ma/cl) prn buf cod&car ofs  I_20   Q_20    delta cod / car       distance
*  1 ( 0/11) 28 -1  0.000    0
  11 ( 1/12) 28  0  0.000  118   -730 -23826      0.000 /   -0.309      0.0      0.000
  12 ( 1/ 0) 28  1  0.000 -118 -22595  -8205     -0.000 /    0.588      0.0      1.000

--- | r : redraw | q : quit ogdspl | +/- : cycle pages | ---
```

Figure 5. Screen shot of a terminal window running the "OpenGPS" user space application `ogdspl`. In the lower half characteristic information on the 12 tracking channels is shown. Note that `ogdspl` maps azimuth angles to the interval $[-180°, +180°]$ with $-90°$ and $+90°$ referring to west and east, respectively. At the time of the measurement on 16 October 2015 channel 1 tracked PRN 28 at an elevation angle of $+1.64°$ (column 6 entitled "elev"). Its azimuth value ($-98.15°$) is within the selected observation window ($[-160°, -20°]$) and the O/L channels A and B, here listed as channel 11 and 12, are cloned from channel 1. In-phase and quad-phase samples as well as parameters describing the alignment between master and clone channels are listed at the very bottom of the screen. The top few lines list position and clock solutions from to the real-time navigation solution.

loops. To maintain tracking lock the carrier phase and code data have to be read from the GP2021 registers, the necessary loop adjustments have to be determined and written back to the correlator within a time interval of less than 100–200 μs. The real-time extension layer RTAI guarantees this latency performance even for high disk reading/writing operations or network traffic. `ogrcvr` handles deferrable tasks, such as determination of satellite positions and velocities from ephemeris data, calculation of the navigation solution and data storage. Communication between real-time module and user space process is accomplished using shared memory and FIFO (first in, first out) buffers. Inspection and modifications of relevant signal tracking parameters, such as loop bandwidths and loop orders, O/L channel frequency and code offsets, sampling frequencies, are performed via a `proc`-based command line interface.

A third process, `ogdspl`, can optionally be started to display tracking and positioning information on the terminal screen (fig. 5). In total, the source code of all kernel and user space modules comprises about 20,000 lines of C code.

The "OpenGPS" receiver operates in two different observation modes. In "monitor mode" up to 10 of the 12 correlator channels are assigned to PRNs of visible GPS satellites. The O/L channels A and B, in fig. 5 listed as number 11 and 12, remain unassigned. When a satellite, tracked by channel number k, crosses the $+2°$ elevation boundary from above, the receiver transitions to “measurement mode”, channels A and B are assigned to this satellite’s PRN and their code and carrier NCOs are aligned to those of channel k as well. In the following this process is called “cloning” of A and B from the “master” channel k and A/B are referred to as “clone” channels.

In “measurement mode” code and carrier NCO data, in-phase and quad-phase correlation sums from both GP2021 correlation branches (“prompt” and “dither”), as well as position and clock bias results from the real-time navigation solution are stored on the local hard disk. The delay between the prompt and dither branch is fixed at 0.5 chips (about 150 m). Code, carrier phases and correlation sums are written with a temporal resolution of $T_s = 0.02$ ms (corresponding to a sampling frequency of $f_s = 50$ Hz), the navigation solution is provided once per second. We note that the stored correlation sums are coherently integrated over T_s, whereas the NCO code and carrier phase are instantaneous values sampled at the corresponding “TIC” event.

Typically, “measurement mode” lasts for about 10–15 minutes and ends when the satellite’s elevation angle drops below $-2°$. During an initialization phase, for elevation angles above $0°$, the code and carrier phase loop adjustments are collected at each “TIC” event and stored. Thereafter, when elevation angles are below $0°$, the carrier loop is opened and NCO input values are calculated by linear extrapolation of the stored Doppler adjustments. For code O/L tracking a hybrid method is employed; if $C/N_0 \leq 30$ dB Hz, the code NCO values are calculated from a second-order polynomial extrapolation of the stored adjustments. Otherwise, the code loop operates in C/L mode; in addition, the difference between actual adjustments and model-derived values is saved and added to the model. Thus, potential deviations between observations at $C/N_0 > 30$ dB Hz and the extrapolated loop adjustments are used to update the model.

The “OpenGPS” receiver software determines geometric elevation angles from GPS almanac information. Since the data post-processing analysis is based on the more precise GPS ephemeris data, the elevation angles of the measurement start and the end of the O/L initialization may deviate from the nominal values of $+2°$ and $0°$, respectively, by some tenths of a degree (see, e.g., insert in fig. 3).

We end this section with a comment on the O/L implementation used by “OpenGPS” receiver. Compared to O/L methods employed by space-based GNSS-RO receivers, which are based on predetermined code and carrier parameters derived from atmospheric climatologies (Sokolovskiy, 2001; Sokolovskiy et al., 2006; Ao et al., 2009; Bonnedal et al., 2010), the “OpenGPS” O/L technique, creates a different O/L model during the initialization phase (elevation angles between $+2°$ and $0°$) for each setting event. Thus, diurnal variations in the atmospheric refractivity field may be better accounted for in the O/L model. On the other hand, under high-humidity conditions strong refractivity gradients could lead to SNR fluctuations and subsequent (transient) loss of tracking lock already during the O/L initialization phase at positive elevation angles producing a faulty O/L model. In this case it is possible that C/L tracking actually outperforms the O/L results (see discussion below and fig. 7).

3 Measurements

Within the framework of the “GLESER” campaign, which started in December 2010, low-elevation setting events are observed. Since that date the data acquisition runs almost continuously. However, gaps of up to several days are caused by hardware or

Atmos. Meas. Tech. Discuss., doi:10.5194/amt-2016-59, 2016
Manuscript under review for journal Atmos. Meas. Tech.
Published: 18 April 2016

Atmospheric Measurement Techniques
Discussions
Open Access

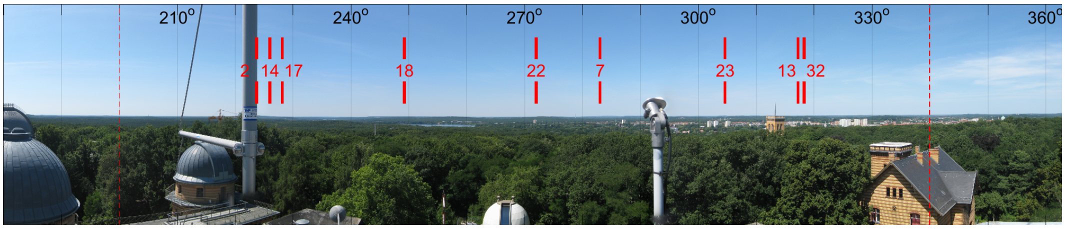

Figure 6. View towards west from the observation platform. The picture was taken about 2–3 m behind the receiver's GPS antenna which is tilted by about 45° towards west (the antenna and its mounting pole is visible at about 290° azimuth angle). The metal structure at about 220° is part of a lightning protection system and does not block the antenna's field of view which ranges from 200° to 340°. Throughout the observation period a satellite with a given PRN sets beyond the horizon at almost the same azimuth angle. The angles of those nine PRNs discussed in the present study are marked in red.

software problems, operator errors or other technical reasons. The following discussion is restricted to observations recorded in 2014. The instrument provided on average 8.3 observations per day throughout this year with three data gaps (29 January to 1 February, 29–31 August and 18–22 December 2014). Between 15 July and 6 September the "OpenGPS" receiver malfunctioned due to an operator error and 437 observations from that time period are removed from the data set leaving 2581 low-elevation events.

The instrument is housed on the top floor of the former water tower on the "Albert Einstein" science campus in Potsdam, Germany (52.3808°N, 13.0642°E). An active L1(1575.42 MHz) GPS antenna (NovAtel/ANTCOM 2G15A-XTB) is mounted on the tower's observation deck and tilted by about 45° towards the western horizon to increase recorded signal strength at very low elevation angles. The antenna includes a low-noise amplifier with 33 dB gain and is sensitive to RHCP polarization only. A 10 m low-loss signal cable connects the antenna to the "OpenGPS" receiver. According to the manufacturer's documentation the cable loss is 14 dB per 100 m at 1 GHz.

Fig. 6 depicts the panoramic view of the western horizon from the observation deck between azimuth angles of 180° (south) and 360° (north). The azimuth angles are marked in black at the top side of the photograph. Thick red lines indicate the azimuth angles of those PRNs which are analyzed in the present study. The picture was taken a few meters east of the receiving patch antenna, which is visible to the right of the 290° azimuth tick mark.

Data acquisition is activated once a satellite enters the observation window which ranges from $+200^\circ$ to $+340^\circ$ in azimuth (thin broken red lines in fig. 6) and from $+2^\circ$ to -2° in elevation. Any additional satellite entering the observation window during this time period, is disregarded and not tracked in O/L mode. Raw observables stored on disk include pseudoranges $\rho_{\mathrm{C/L},n}$, carrier phases $\varphi_{\mathrm{C/L},n}$ and time tags t_n for all C/L channels. In addition, raw O/L measurements (in-phase and quad-phase correlation sums $\tilde{I}_n$ and $\tilde{Q}_n$, NCO ranges $\rho_{\mathrm{NCO},n}$ and NCO carrier frequencies $f_{\mathrm{NCO},n}$ from both O/L channels) are written to separate files. Here, the subscript $n = 1, 2, \ldots$ enumerates the successive "TIC" events recurring every 20 ms. The correlation sums $\tilde{I}_n$ and $\tilde{Q}_n$ are not sampled at "TIC" instants, but are coherently integrated over a time period of 20 ms preceding the

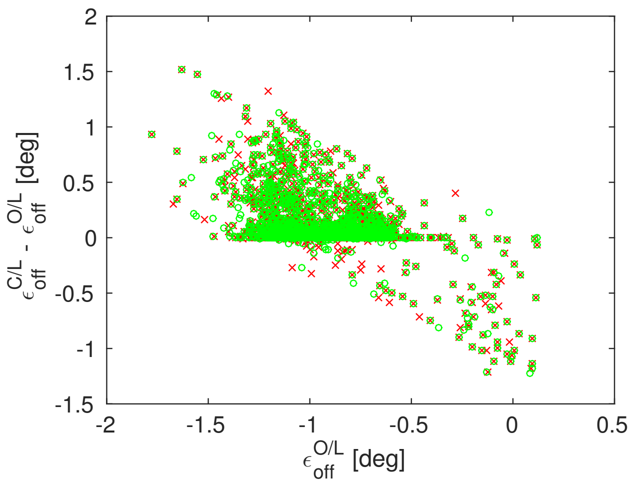

Figure 7. Open-loop performance in terms of the gain or loss in elevation angle range compared to closed-loop tracking. The end elevations $\epsilon_{\mathrm{off}}^{\mathrm{O/L}}$ and $\epsilon_{\mathrm{off}}^{\mathrm{C/L}}$ are the lowest elevation angles with C/N$_0$ still exceeding 30 dB Hz. In general, O/L tracking lowers the final elevation angle by about 0.11° on average. However, in about 14% of the measurements C/L tracking outperforms the O/L channels, in a few cases by up to 1°. Red markers refer to O/L channel A, green to channel B.

"TIC" event. The corresponding time offset between $\tilde{I}_n$, $\tilde{Q}_n$ and $\varphi_{\mathrm{NCO},n}$ are disregarded in the following analysis. Raw data accumulation rate is about 360 MByte per day or about 2.5 GByte per week.

In order to quantify the performance gain of O/L in comparison to C/L detection we compare in fig. 7 the lowest elevation angles observed in the two tracking modes, $\epsilon_{\mathrm{off}}^{\mathrm{O/L}}$ and $\epsilon_{\mathrm{off}}^{\mathrm{C/L}}$. They are defined as the minimum elevation in a given setting event with the smoothed density ratio C/N$_0$ still exceeding 30 dB Hz. Smoothing is performed by a running mean filter of 1 s width. We find that out of a total of 2581 setting events 2368 and 2366 were recorded by the O/L channel A and B, respectively. In the remaining 8% of the observations closed-loop tracking stopped too early and O/L was never activated. With active channels A and B, on the other hand, in about 86% of the O/L measurements (2017 out of 2368 and 2069 out of 2366 for channel A and B, respectively) end elevation angles from O/L tracking yielded smaller values compared to the C/L results. And in 21% of the measurements (499 out of 2368 and 505 out of 2366 for channel A and B, respectively) O/L tracking extended more than 0.25° further down than the corresponding C/L observation.

4 Data Processing and Analysis

Data processing is performed on an event-by-event basis. Typically, setting events last about 700–900 s; however, measurements extending over a time period of up to 1400 seconds are occasionally observed. During the initial stage "OpenGPS" raw data files are converted to MATLAB® binary format to facilitate the subsequent processing steps. First, the observed in-phase and quad-phase samples sums are demodulated

$$\begin{aligned} I_n &= D_n \tilde{I}_n \\ Q_n &= D_n \tilde{Q}_n \end{aligned} \tag{1}$$

to allow calculation of the residual phase samples

$$\varphi_{\text{res},n} = \text{atan2}(Q_n, I_n) \quad . \tag{2}$$

Here, the four-quadrant arctangent atan2(x,y) denotes the principal value of the angle of the complex number $x + iy$.

The literature discusses two methods for the determinatio of the data bits D_n, "internal" and "external" demodulation. On the one hand, D_n can be extracted from the observations $\tilde{I}_n$ ands $\tilde{Q}_n$ themselves (Sokolovskiy et al., 2009). Alternatively, external demodulation extracts D_n from independent observations, such as GFZ's "NavBit" data base (Beyerle et al., 2009). In the following external demodulation is used since in low-elevation events the modulus of the difference between adjacent the carrier phase residuals, $|\varphi_{\text{res},n} - \varphi_{\text{res},n-1}|$ frequently reach and exceed $\pm 90°$. In these cases a clear separation between propagation-induced phase fluctuations and phase changes due to a sign change of D_n is difficult to achieve.

Accumulated residual carrier phase samples $\Phi_{\text{res},n}$ then follow from

$$\Phi_{\text{res},n} \equiv \varphi_{\text{res},n} + C_n = \text{atan2}(Q_n, I_n) + C_n \tag{3}$$

with the unwrapping term C_n defined by

$$C_n = \begin{cases} C_{n-1} + 2\pi & : \ \text{atan2}(Q_n, I_n) - \text{atan2}(Q_{n-1}, I_{n-1}) < -\pi \\ C_{n-1} - 2\pi & : \ \text{atan2}(Q_n, I_n) - \text{atan2}(Q_{n-1}, I_{n-1}) > +\pi \\ C_{n-1} & : \ \text{else} \end{cases} \tag{4}$$

if $n > 1$ and $C_{n=1} = 0$ (Beyerle et al., 2011). In addition, during this first processing stage the receiver's 1 Hz navigation solution, which includes an estimate of the receiver's clock bias, is retrieved as well.

Second, elevation and azimuth angles for each tracked satellite are calculated from broadcast ephemeris data using the bias-corrected receiver clock time and linearly interpolated from 1 Hz to 50 Hz. From the bit-corrected phase samples $\Phi_{\text{res},n}$ the observed carrier frequencies

$$\begin{aligned} f^{(A,B)}_{\text{obs},n} &\equiv f^{(A,B)}_{\text{NCO},n} + f^{(A,B)}_{\text{res},n} \\ &\approx f^{(A,B)}_{\text{NCO}} + \frac{1}{2\pi} \frac{\Phi^{(A,B)}_{\text{res},n} - \Phi^{(A,B)}_{\text{res},n-1}}{t_n - t_{n-1}} \end{aligned} \tag{5}$$

are derived with superscript A and B indicating the corresponding O/L channel. Fig. 8 shows $f^{(A,B)}_{\text{obs},n}$ (eqn. 5) corresponding to the event plotted in fig. 3 using external data bit demodulation (red and green lines). The C/L channel (blue line) loses lock at about $-0.3°$ elevation and its carrier frequency output leaves the scale. Incidentally, at about $-1.2°$ the C/L frequency briefly crosses the displayed frequency range again. Below about $-1.2°$ elevation Earth's limb completely shadows the signal from PRN 7 (see fig. 2) and from there on O/L and C/L outputs contain noise only.

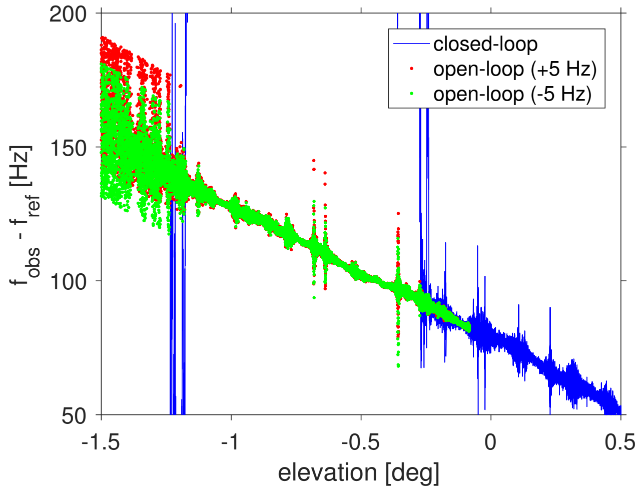

Figure 8. Observed carrier frequencies f_{obs}, reconstructed from NCO and residual frequencies (eqn. 5), using external data bit demodulation as a function of elevation angle (red and green). In addition, the closed-loop result is plotted in blue. For clarity, a constant offset $f_{\text{ref}} = 1.4071$ MHz is subtracted. Same event as shown in figs. 2 and 3.

In addition, with the observed in-phase and quad-phase correlation sums, $\tilde{I}_n$ and $\tilde{Q}_n$ (eqn. 1), the signal-to-noise density ratio C/N$_0$ in units of dB Hz is calculated according to

$$\text{C/N}_0(\text{dB Hz}) \quad = \quad 10 \cdot \log\left(\frac{\left\langle \tilde{I}^2 + \tilde{Q}^2 \right\rangle}{2 \cdot \text{Var}\left(\tilde{Q}^{\text{C/L}}\right) \cdot T_c}\right) \tag{6}$$

Here, $\langle x \rangle$ is the mean value of x and $T_c = 0.02$ s denotes the coherent integration time. Var$\left(\tilde{Q}^{\text{C/L}}\right)$ is the variance of the observed quad-phase correlation sums of the associated master channel running in C/L mode between $0°$ and $+2°$ elevation angle.

If no GPS signal is present and the receiver input signal is pure noise, $\tilde{I}$ and $\tilde{Q}$ are uncorrelated and

$$\left\langle \tilde{I}^2 + \tilde{Q}^2 \right\rangle = 2 \cdot \left\langle \tilde{Q}^2 \right\rangle = 2 \cdot \text{Var}\left(\tilde{Q}\right) \approx 2 \cdot \text{Var}\left(\tilde{Q}^{\text{C/L}}\right) \tag{7}$$

since $\left\langle \tilde{Q} \right\rangle = 0$. Under these conditions the density ratio C/N$_0$(dB Hz) assumes the noise level of

$$10 \cdot \log\left(\frac{1}{T_c}\right) \approx 17 \text{ dB Hz} \tag{8}$$

using eq. 6 (dashed black line in fig. 2).

Atmos. Meas. Tech. Discuss., doi:10.5194/amt-2016-59, 2016
Manuscript under review for journal Atmos. Meas. Tech.
Published: 18 April 2016

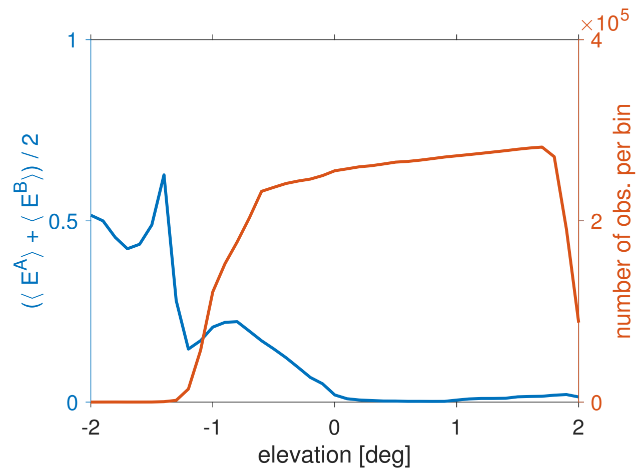

Figure 9. Success rate of internal navigation bit retrieval in terms of averaged performance parameter $\langle E \rangle$ (eqn. 9) as a function of elevation angle for signal density ratios C/N$_0$ $\geq$ 30 dB Hz (blue, left axis). The corresponding number of observations per elevation bin is plotted as well (red, right axis). The statistics is based on 242 observations recorded in January 2014.

5 Discussion and Interpretation

We begin the discussion of the "GLESER" results by comparing the performance of internal versus external data bit demodulation and define the quantity

$$E_n^{\mathrm{X}} \equiv \left| |D_n^{\mathrm{X,int}} - D_{n-1}^{\mathrm{X,int}}| - |D_n^{\mathrm{ext}} - D_{n-1}^{\mathrm{ext}}| \right| \tag{9}$$

Here, $|x|$ denotes the modulus of x, the superscript $X = A$ or $X = B$ indicates the O/L channel and "int"/"ext" characterizes the demodulation method. The quantity E_n^X is sensitive to differences between sign changes from one sample to the next, rather than differences between the bit values, since only the former affect the derived carrier frequency. We note that $\langle E_n^{\mathrm{X}} \rangle = 1$ for randomly chosen $D_n^{\mathrm{X,int}}$ and D_n^{ext}.

For 242 observations in January 2014 with signal density ratios C/N$_0$ $\geq$ 30 dB Hz the parameters E_n (eqn. 9) are grouped into an elevation grid with $0.1°$ bin size and averaged. The result is shown in fig. 9. For elevation angles just below $0°$ there is good agreement between internal and external data bit retrieval; for lower elevations, however, the success rate decreases significantly. Results for elevation angles below $-1.2°$, however, are statistically not significant due to the strongly decreasing number of observations (red line). To eliminate potential errors caused by internal data bit removal, we restrict the following discussion to data processed using external demodulation.

Table 1 lists all 19 PRNs recorded during the 311 day observation period in 2014 and the corresponding number of setting events. The third column gives the mean azimuth angle and its 1-σ standard deviation at $0°$ elevation. Enhanced changes in azimuth angle of PRN 8 are most likely related to the decommissioning of GPS space vehicle number 38 in October 2014. The last column in table 1 shows the fractions of profiles in which O/L tracking reached a lower elevation angle than the

Table 1. Number of low-elevation events and azimuth angle at zero elevation for all 19 PRNs recorded during 311 days in 2014. Azimuth angle is given as mean and 1-σ standard deviation. The last column lists the percentages of observation in which O/L tracking reached a lower elevation angle than the corresponding C/L detection. The first number refers to O/L channel A, the second to channel B.

PRN	number of events	azimuth at zero elev. [deg]	O/L enhancement [%]
2	153	223.8 ± 1.0	98.6 / 97.3
4	71	201.9 ± 0.4	91.2 / 94.1
6	99	203.4 ± 1.0	97.7 / 97.7
7	174	283.1 ± 1.4	96.4 / 97.0
8	41	271.4 ± 18.3	94.4 / 97.2
9	70	325.3 ± 0.4	72.1 / 82.0
12	112	332.4 ± 1.9	57.0 / 61.3
13	202	317.2 ± 4.6	88.1 / 91.7
14	182	226.0 ± 0.6	99.4 / 99.4
17	168	228.2 ± 1.3	73.9 / 85.1
18	168	249.3 ± 1.1	100.0 / 98.8
21	118	296.6 ± 1.9	70.5 / 75.0
22	169	272.0 ± 1.7	95.2 / 96.4
23	222	304.6 ± 1.5	87.8 / 88.2
28	172	260.2 ± 0.2	34.3 / 35.5
29	30	315.9 ± 0.5	66.7 / 63.3
30	29	298.8 ± 0.1	96.4 / 100.0
31	177	206.2 ± 1.2	98.9 / 98.9
32	224	318.3 ± 1.1	70.3 / 75.1

corresponding C/L result. E.g., a value of 70% indicates that in 30 out of 100 observations the C/L channel tracked to lower elevation than the corresponding O/L channels.

The panorama photograph (fig. 6) shows the view to the local horizon within the 140° wide observation window ranging from 200° to 340° and centered at 270° azimuth (west). It exhibits a substantial variation of surface properties in azimuth angle with enhanced building densities of the city of Potsdam in westerly to northwesterly direction (about 280° to 350°), mostly forests at azimuth angles below 270° and water surfaces from lake "Templiner See" between about 250° and 260°. Also indicated in fig. 6 are the approximate zero-elevation azimuth angles of setting GPS satellites (red marks). Due to the specific geometry of the GPS constellation the orbit traces exhibit a characteristic azimuth angle repeat pattern when viewed from a fixed ground-based location (Axelrad et al., 2005; Choi et al., 2004). I.e., a specific PRN sets at the same azimuth angle with small deviations of less than one degree (cf. centre column of table 1).

In the following the observation are grouped PRN-wise. The azimuth angle repeat pattern implies that these subsets refer to almost the same azimuth angles. For example, the setting of PRN 18 invariably takes places at lake “Templiner See”, whereas PRN 32 sets across the urbanized area of Potsdam throughout the year. The non-uniform topography is the most likely explanation for the observed variability in C/N$_0$ (see, e.g., fig. 2) and, as will be discussed below, Doppler frequency with respect to azimuth angle. The occurrence time of the setting event, however, shifts by about 4 minutes per day, which corresponds to 24 h per average year (365.25 days). Thus, the statistical analysis performed in the present study essentially averages out any potential diurnal variation. The investigation of these variations is left to future research.

Fig. 10 provides a general overview of the observed mean signal density ratios

$$\mathrm{C/N}_0^{\mathrm{avg}}(\mathrm{dB\ Hz}) \equiv \frac{1}{2}\left(\mathrm{C/N}_0^A(\mathrm{dB\ Hz}) + \mathrm{C/N}_0^B(\mathrm{dB\ Hz})\right) \tag{10}$$

as a function of elevation angle. We note that by expressing C/N$_0$ in units of dB Hz, eqn. 10 constitutes in effect a geometric mean value in terms of the ratios $\left\langle \tilde{I}^2 + \tilde{Q}^2 \right\rangle / \left(2 \cdot \mathrm{Var}(\tilde{Q}^{\mathrm{C/L}}) \cdot T_c\right)$ (see eqn. 6). Fig. 10 shows C/N$_0$ for PRNs 2, 7, 13, 14, 17, 18, 22, 23 and 32. The following analysis is focused on this set of nine PRNs; they were selected according to data availability and azimuth angle coverage. The individual panels in fig. 10 and the following figures are arranged row-wise according to increasing azimuth angle (cf. fig. 6). In fig. 10 also the mean and 1-σ standard deviations are plotted with an elevation bin size of 0.2° (blue). The overall features are similar in all nine panels with C/N$_0$ $\approx 40 - 45$ dB Hz at the start of the setting event decreasing to about 15 dB Hz at the lower end. At about 0° elevation, at the transition between C/L and O/L tracking, signals propagation over the urban area (PRNs 23, 13 and 32 corresponding to azimuth angles of 305°, 317° and 318°) appear to exhibit stronger C/N$_0$ attenuations and fluctuations compared to signals arriving from more southerly directions across forest areas.

Examining density ratio averages (eqn. 10) in lieu of C/N$_0^A$ and C/N$_0^B$ is justified, since the two values agree in the majority of observations. As a matter of principle, however, significant deviations are conceivable, because the density ratio depends on frequency offset $\Delta f^{(A,B)}$ between the O/L NCO frequency $f_{\mathrm{NCO}}^{(A,B)}$ and the signal's true carrier frequency f_0,

$$\Delta f^{(A,B)} \equiv f_{\mathrm{NCO}}^{(A,B)} - f_0 \quad . \tag{11}$$

Provided the observed and replica signal are perfectly aligned in the pseudorange domain, the amplitude loss induced by $\Delta f^{(A,B)}$ is given by

$$L(\Delta f^{(A,B)}) \equiv \left| \frac{\sin(\pi\,\Delta f^{(A,B)}\,T_c)}{\pi\,\Delta f^{(A,B)}\,T_c} \right| \tag{12}$$

with a coherent integration time of T_c. For illustration fig. 11 shows the normalized C/A code correlation function as a function of code lag and frequency offset in the vicinity of the correlation maximum and the loss function $L(\Delta f^{(A,B)})$ at zero delay (red line).

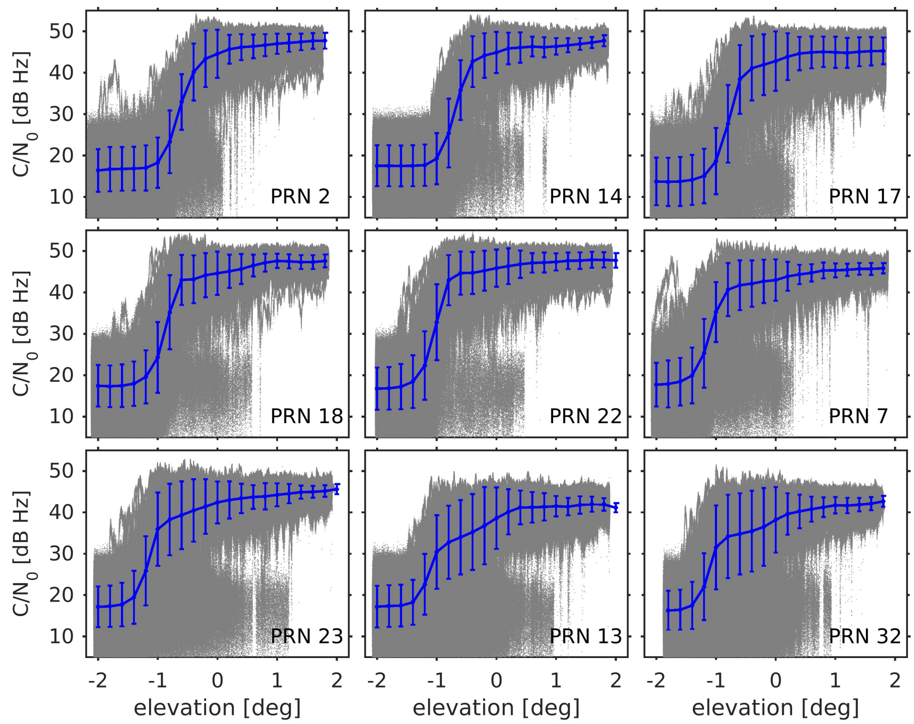

Figure 10. Carrier signal-to-noise density ratio, averaged over the two O/L channels, as a function of elevation angle. The panels show observation from nine PRNs sorted row-wise according to increasing azimuth angle (cf. fig. 6). Mean and 1-σ standard deviations, calculated from $0.2°$ elevation bins, are marked in dark blue. The noise level is reached at about 17 dB Hz (see eqn. 8).

Thus, in the absence of other factors affecting $\mathrm{C/N}_0^A$ and $\mathrm{C/N}_0^B$ individually, the density ratios of channel A and B will differ by

$$\begin{aligned}\Delta\mathrm{C/N}_0 &\equiv \mathrm{C/N}_0^A - \mathrm{C/N}_0^B \\ &= 20\log\left|\frac{\Delta f^{(B)}}{\Delta f^{(A)}}\,\frac{\sin(\pi\,\Delta f^{(A)}\,T_c)}{\sin(\pi\,\Delta f^{(B)}\,T_c)}\right| \quad .\end{aligned} \tag{13}$$

The statistics of $\Delta\mathrm{C/N}_0$ is plotted in fig. 12 as a function of elevation angle. Mean density ratio values, grouped in steps of $0.2°$, are marked in blue with error bars indicating the 1-σ standard deviation. The mean values of $\Delta\mathrm{C/N}_0$ are zero within the statistical uncertainties; individual observations, however, experience differences of more than 10 dB Hz. While in general the largest deviations occur below $0°$ elevation, i.e. during O/L tracking, also C/L tracking results exhibit non-zero values of $\Delta\mathrm{C/N}_0$. Finally, in the panels for PRNs 7, 22 and 23 characteristic features between $-1°$ and $0°$ elevation are evident. Their most likely explanation are multipath signal propagation at azimuth angles between about $270°$ to $300°$.

Atmos. Meas. Tech. Discuss., doi:10.5194/amt-2016-59, 2016
Manuscript under review for journal Atmos. Meas. Tech.
Published: 18 April 2016

Atmospheric Measurement Techniques Discussions
Open Access

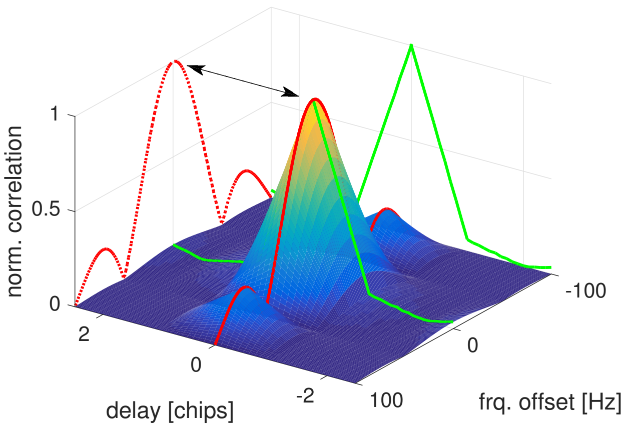

Figure 11. Normalized C/A code correlation function as a function of delay and Doppler frequency offset. At zero delay the code correlation function corresponds to the frequency response (solid red line). It closely matches the modulus of the normalized sinc function (dotted red line, shifted by $+2.5$ chips for clarity).

The observed density ratio difference $\Delta\mathrm{C/N_0}$ can be analyzed quantitatively. For this, the observation $f_{\mathrm{obs}}^{(A,B)} \approx f_0$ is assumed to be a valid approximation for the true carrier frequency f_0. Using the defining eqn. 5 we obtain

$$f_{\mathrm{obs}}^{(A)} - f_{\mathrm{obs}}^{(B)} = \left(f_{\mathrm{NCO}}^{(A)} + f_{\mathrm{res}}^{(A)}\right) - \left(f_{\mathrm{NCO}}^{(B)} + f_{\mathrm{res}}^{(B)}\right) \approx 0 \tag{14}$$

and

$$\Delta\mathrm{C/N_0}(f_{\mathrm{res}}^{(A)}) \quad \approx \quad 20\log\left|\frac{f_{\mathrm{res}}^{(A)} + 10\,\mathrm{Hz}}{f_{\mathrm{res}}^{(A)}} \; \frac{\sin\left(\pi\, f_{\mathrm{res}}^{(A)}\, T_c\right)}{\sin\left(\pi\,(f_{\mathrm{res}}^{(A)} + 10\,\mathrm{Hz}\right)\, T_c)}\right| \tag{15}$$

or, alternatively,

$$\Delta\mathrm{C/N_0}(f_{\mathrm{res}}^{(B)}) \quad \approx \quad 20\log\left|\frac{f_{\mathrm{res}}^{(B)}}{f_{\mathrm{res}}^{(B)} - 10\,\mathrm{Hz}} \; \frac{\sin\left(\pi\,(f_{\mathrm{res}}^{(B)} - 10\,\mathrm{Hz})\,T_c\right)}{\sin\left(\pi\, f_{\mathrm{res}}^{(B)}\, T_c\right)}\right| \quad . \tag{16}$$

Figure 13 shows the correlation between the observed density ratio differences $\Delta\mathrm{C/N_0}$ and $f_{\mathrm{res}}^{(A)}$ (gray data points). Here, the data set is restricted to the subset of typically 200,000 to 350,000 samples tracked in O/L mode. The expected result derived from equation 15 is overlaid in dark blue, dashed lines mark the residual frequency of -5 Hz.

The resulting patterns exhibit a marked dependence on PRN, i.e. on azimuth angle. Whereas the observations of PRN 14 (azimuth angle at about 226°) indicate only moderate excursions in terms of residual frequency with most data points clustered at -5 Hz (dashed line), the signals from PRN 32, arriving from an azimuth angle of 318°, show strong deviations causing residual frequencies exceeding the Nyquist value of $f_s/2 = 25$ Hz. Here the agreement with the theoretical results (blue line, eqn. 15) is evident. A substantial number of observations deviate from the O/L model by more than $f_s/2$ and are therefore

Atmos. Meas. Tech. Discuss., doi:10.5194/amt-2016-59, 2016
Manuscript under review for journal Atmos. Meas. Tech.
Published: 18 April 2016

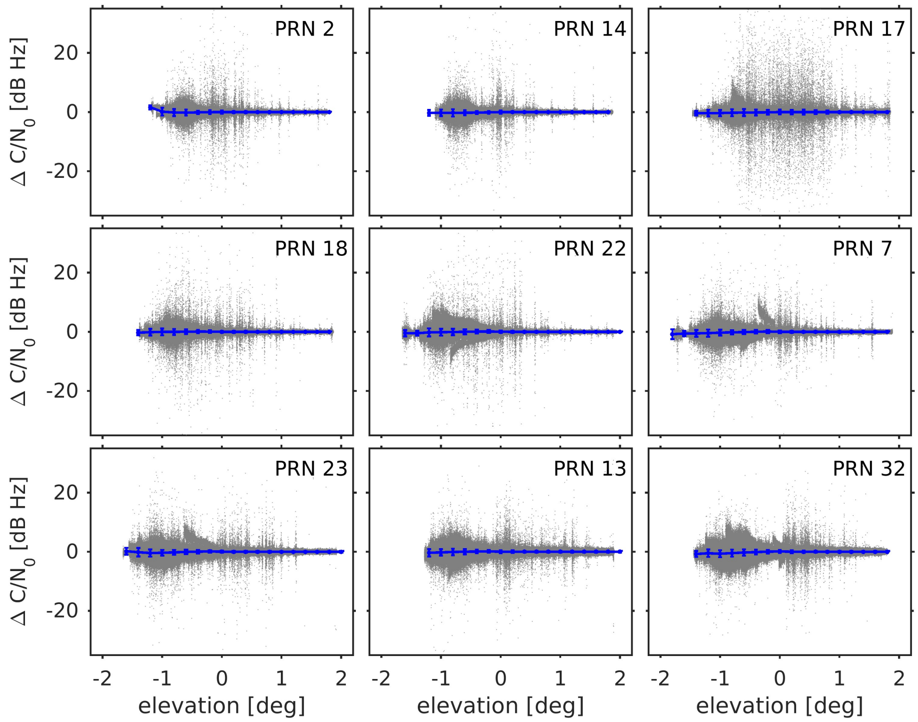

Figure 12. Same as fig. 10, however, showing $\Delta C/N_0$, the difference of the two O/L density ratios, as a function of elevation angle.

affected by aliasing. The light blue curves, which are derived from eqn. 15, but shifted by ± 50 Hz, show good agreement with the observations and substantiate this interpretation. The aliasing effect it stronger for negative $f_{\text{res}}^{(A)}$ since channel A is shifted with respect to the O/L model by an additional -5 Hz.

Correspondingly, aliasing for positive residual frequencies is stronger for channel B since this channel is shifted with respect to the O/L model by $+5$ Hz as is illustrated with fig. 14 which shows the corresponding result derived O/L channel B data. Again, the dark blue lines (and the aliased curves in light blue) mark the theoretical result derived from eqn. 16.

The preceding discussion is based on the assumption

$$f_{\text{obs}}^{A} \quad = \quad f_{\text{obs}}^{B} \quad . \tag{17}$$

Referring to fig. 15, however, we deduce that eqn. 17 is not strictly fulfilled, in particular for low density ratios. The panels in fig. 15 show the the observed frequency difference $\Delta f_{\text{obs}} \equiv f_{\text{obs}}^{(A)} - f_{\text{obs}}^{(B)}$ as a function of mean density ratio for the selected nine PRNs. Their mean values and 1-σ standard deviations, sorted into 2.5 dB Hz bins, are superimposed on the individual data points (gray dots) as dark blue lines.

Atmos. Meas. Tech. Discuss., doi:10.5194/amt-2016-59, 2016
Manuscript under review for journal Atmos. Meas. Tech.
Published: 18 April 2016

Atmospheric Measurement Techniques
Discussions
Open Access

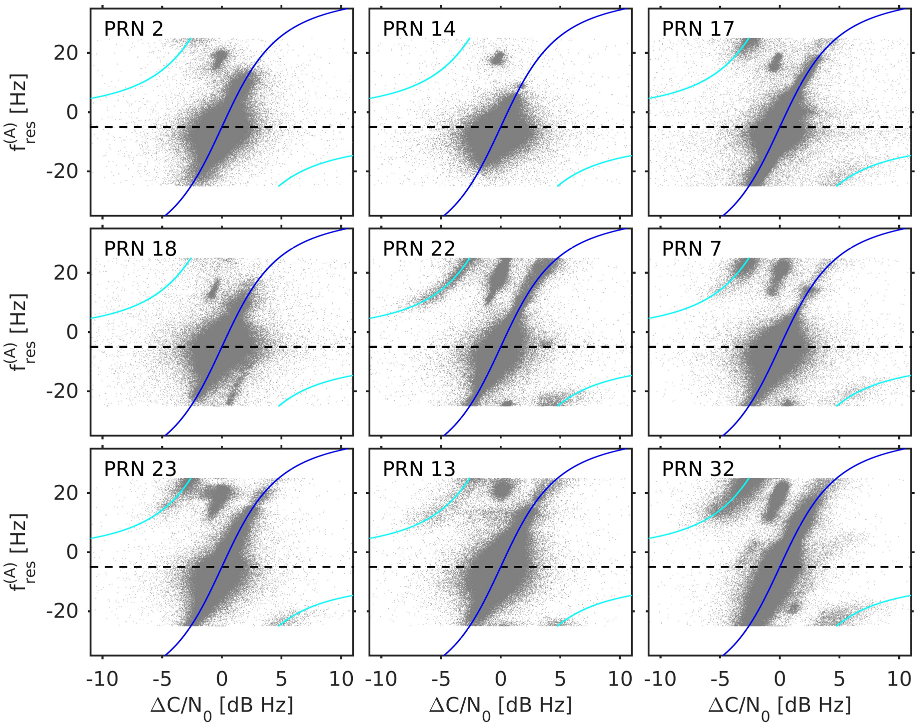

Figure 13. Same as fig. 10, however, showing the residual frequency in O/L channel A as a function of $\Delta C/N_0$, the difference of the two O/L density ratios. For details see text.

In all panels a small fraction of the data set, denoted by $\rho_{40\,\mathrm{Hz}}$ in fig. 15, populates the frequency band $\Delta f_{\mathrm{obs}} \gtrsim +40$ Hz with a mean value of about $+50$ Hz and signal levels ranging from 10–20 dB Hz to more than 40 dB Hz. Again, this $+50$ Hz offset is caused aliasing. If the true signal frequency f_0 occurs within the frequency range between $+20$ to $+25$ Hz, it is correctly tracked by channel A, but aliased to the -30 Hz to -25 Hz frequency window by channel B, since channel B's NCO is shifted by -10 Hz with respect to channel A's NCO and therefore its frequency range extends from -30 Hz to $+20$ Hz. Thus, the frequencies observed by channel A and B will differ by $+50$ Hz. Conversely, signals appearing at frequencies between -20 Hz and -25 Hz are properly recorded by channel B, but suffer aliasing from channel A again causing a $+50$ Hz offset in Δf_{obs}. Formally, the observed frequency difference Δf_{obs} as a function of true frequency f_0 is

$$\begin{aligned}\Delta f_{\mathrm{obs}}(f_0) &= \left(f^{(A)}_{\mathrm{NCO}} + f^{(A)}_{\mathrm{res}}(f_0)\right) - \left(f^{(B)}_{\mathrm{NCO}} + f^{(B)}_{\mathrm{res}}(f_0)\right) \qquad (18)\\ &= \begin{cases} 0\ \mathrm{Hz} & : \quad -20\ \mathrm{Hz} < f_0 < +20\ \mathrm{Hz} \\ +50\ \mathrm{Hz} & : \quad \mathrm{else} \quad . \end{cases}\end{aligned}$$

Atmos. Meas. Tech. Discuss., doi:10.5194/amt-2016-59, 2016
Manuscript under review for journal Atmos. Meas. Tech.
Published: 18 April 2016

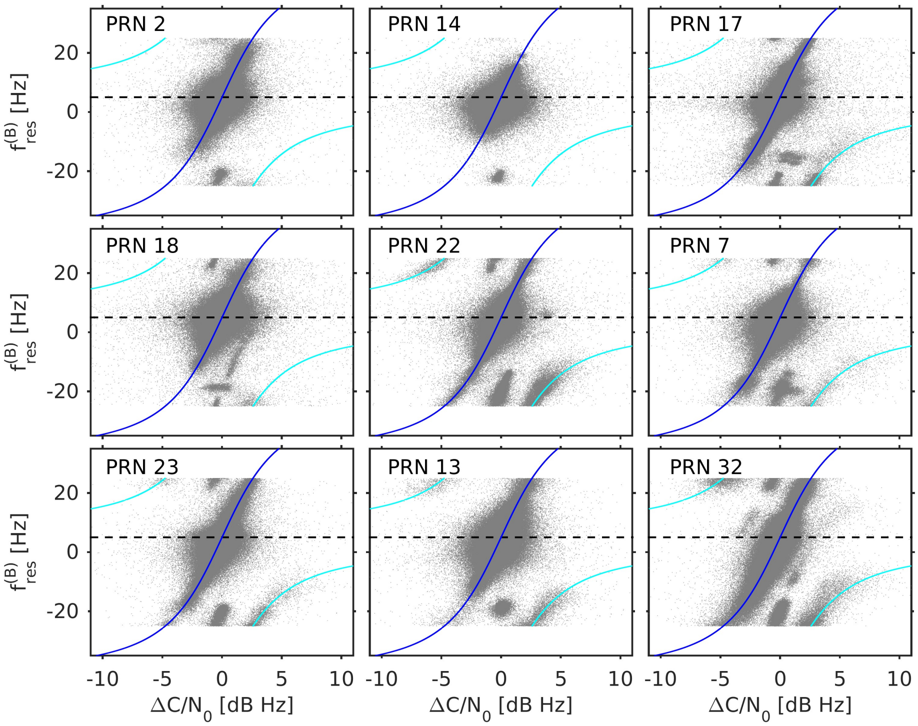

Figure 14. Same as fig. 13, however, showing the corresponding results from O/L channel B.

We note that in both cases the offset is $+50$ Hz and therefore signals differing from f_0 by integer multiples of 50 Hz, cannot be distinguished using our dual-channel O/L technique.

Even though the fraction $\rho_{40\text{ Hz}}$ remains below 4%, the corresponding frequency samples bias the mean value (dark blue line in fig. 15) towards positive frequencies, but they are not the sole cause for the observed bias. If all observations with $\Delta f_{\text{obs}} \geq +40$ Hz are removed from the data set, the corresponding mean values are still biased, albeit significantly less (light blue lines in fig. 15).

The magnitude of the observed frequency bias can be motivated in the following way. In the limit of vanishing signal levels the residual frequencies are dominated by noise and thus

$$f^{(A)}_{\text{res}} \approx 0 \approx f^{(B)}_{\text{res}} \quad . \tag{19}$$

Under these circumstances the observed frequency difference between channel A and B becomes

$$\lim_{\text{C/N}_0 \to \text{noise}} \Delta f = \lim_{\text{C/N}_0 \to \text{noise}} f^{(A)}_{\text{obs}} - f^{(B)}_{\text{obs}} = f^{(A)}_{\text{NCO}} - f^{(B)}_{\text{NCO}} = 10\text{ Hz} \quad . \tag{20}$$

Atmos. Meas. Tech. Discuss., doi:10.5194/amt-2016-59, 2016
Manuscript under review for journal Atmos. Meas. Tech.
Published: 18 April 2016

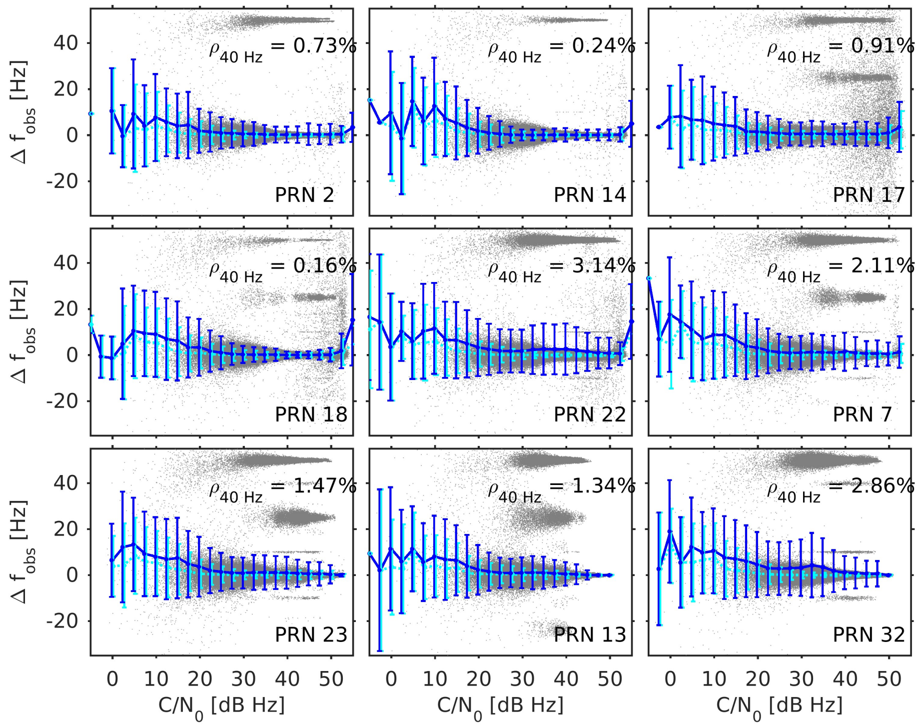

Figure 15. Same as fig. 10, however, showing the difference between the two observed frequencies obtained from O/L channel A and B as a function of the mean signal-to-noise density ratio (eqn. 10). Mean and 1-σ standard deviations, calculated from C/N_0 bins 2.5 dB Hz wide, are marked in dark blue. The fraction of data points exceeding $\Delta f_{\mathrm{obs}} > +40$ Hz is indicated as $\rho_{40\ \mathrm{Hz}}$. The result of the statistical analysis excluding this subset still exhibits a positive bias if $C/N_0 \lesssim 30$ dB Hz (light blue).

The mean values observed in fig. 15 are consistent with this estimate. However, the figure also shows, that for $C/N_0 \gtrsim 30$ dB Hz the frequency difference Δf_{obs} is bias-free; the deviations occur solely at signal levels $C/N_0 \lesssim 30$ dB Hz. We note that this bias is independent from the sampling frequency f_s. The numerical values of C/N_0, though, which characterize the transition zone between biased and bias-free samples, depend on the antenna gain and other receiver-specific parameters. They cannot be directly compared to observations from space-based GNSS-RO payloads which typically are equipped with higher-gain antennas.

Apart from clusters appearing at +50 Hz fig. 15 indicates the presence of frequency offsets at about +25 Hz for PRN 7, 13, 17 and 23. A convincing cause for the presence of these +25 Hz clusters could not be identified; most likely they are related to atmospheric effects on the propagating signal and not receiver-induced, since the effect strongly depends on PRN, i.e. azimuth angle. This issue requires further investigations.

Atmos. Meas. Tech. Discuss., doi:10.5194/amt-2016-59, 2016
Manuscript under review for journal Atmos. Meas. Tech.
Published: 18 April 2016

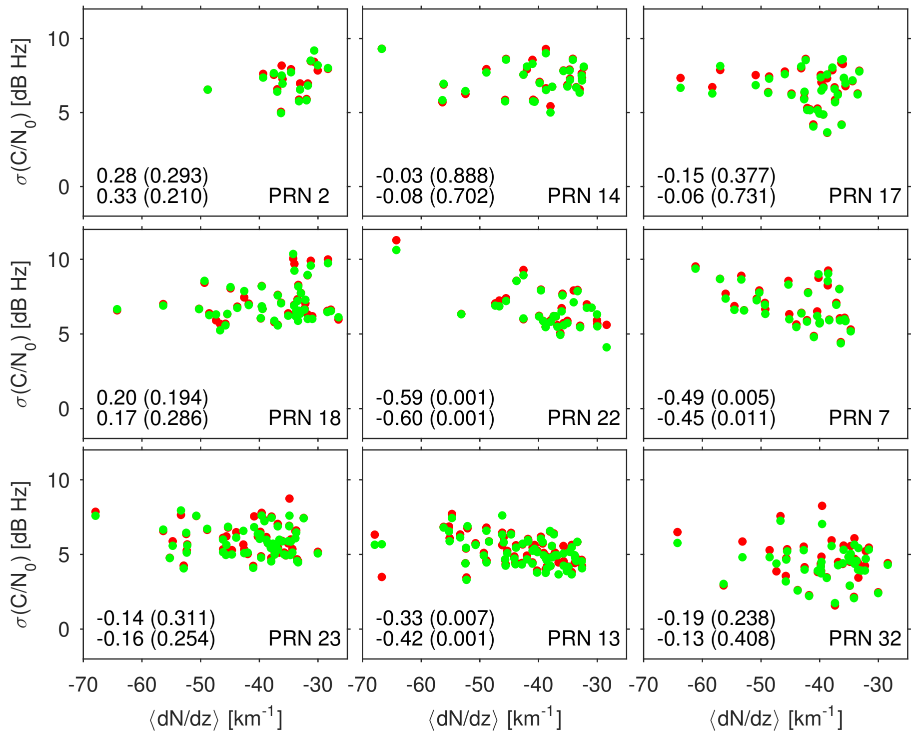

Figure 16. Standard deviation of O/L C/N$_0$ at negative elevation angles versus mean refractivity gradient extracted from ECMWF (March–May 2014). In the lower left corner of each panel the correlation coefficient with the significance parameter in brackets is given (top: channel A, bottom: channel B). In general, consistency is found between results from O/L channel A (red) and channel B (green). Note that only three PRNs (22, 7 and 13) yield significant correlations.

The occurrence of strong SNR fluctuations during the last phase of most setting events (cf. fig. 2) independent of azimuth angle suggest propagation-induced causes in addition to topographic, i.e. surface interaction effects. Hypothetically we relate these fluctuations to multipath ray propagation within the planetary boundary layer. Since multipath propagation presupposes strong vertical refractivity gradients, one would expect an anticorrelation between mean refractivity gradient and the standard deviation of C/N$_0$.

This hypothesis is examined by correlating the mean refractivity gradients $\langle dN(z)/dz \rangle$, averaged over altitudes $z \leq 2$ km, to C/N$_0$ fluctuations. Here, the vertical refractivity profiles $N(z)$ are extracted from European Centre for Medium-Range Weather Forecasts (ECMWF) meteorological fields for the months of March to May 2014. Their horizontal resolution is $1^\circ \times 1^\circ$ (about 100 km $\times$ 100 km) with 137 height levels ranging from 0 to about 80 km; the averaging interval of 0 to 2 km corresponds to about 25 vertical height levels. The signal amplitude fluctuations are taken to be $\sigma(\mathrm{C/N_0})$, the standard deviation of the carrier signal-to-noise density ratios within the elevation range $\epsilon_{\mathrm{off}}^{\mathrm{O/L}} < \epsilon < 0^\circ$.

The correlation result is shown in fig. 16. In the lower left corner of each panel the correlation coefficients with the significance parameters in brackets are displayed. The top entry refers to O/L channel A, the bottom to channel B. Only PRNs 22, 7 and 13 at azimuth angles of 272°, 283° and 317°, respectively, exhibit significant correlations. The statistical analysis reveals an anticorrelation between mean refractivity gradients and C/N_0 fluctuations with correlation coefficients ranging from -0.33 (low correlation) to -0.60 (moderate correlation). An investigation of the relationship between signal amplitude and frequency fluctuations, the local atmospheric refractivity field and, potentially, effects arising from surface topography is beyond the scope of this paper and will be addressed with higher resolution meteorological data in future studies.

6 Conclusions

For more than a decade the "OpenGPS" receiver is used at GFZ in several ground-based and airborne measurement campaigns. Owing to its open hardware and software architecture the device is easily adapted to address specific signal tracking issues in GNSS radio occultation, reflectometry, scatterometry or related fields. Here, a subset of low-elevation events recorded during the long-term "GLESER" campaign are introduced and discussed. Between 1 January 2014 and 31 December 2014 the instrument recorded 2581 validated setting events at an observation site located at 52.3808°N, 13.0642°E. The "OpenGPS" receiver tracks signals from setting GPS satellites simultaneously in both, closed-loop and open-loop mode down to geometric elevation angles of $-1°$ to $-1.5°$. These low-elevation events are characterized by fluctuations of about 10–20 dB Hz in signal-to-noise density ratio and about 10–20 Hz in carrier frequency. Tracking the same event with one closed-loop and two open-loop channels in parallel allows for direct intercomparison of open-loop versus closed-loop performance. Whilst open-loop tracking allows to follow strongly fluctuating signals to very low elevation angles, in about 14% of the observations closed-loop tracking outperformed the open-loop channels, since fluctuations in the early phase of the setting event between $+2°$ and 0° elevation angle prevented proper initialization of the open-loop model.

The analysis of open-loop data is performed on demodulated in-phase and quad-phase correlation samples. The present study suggest that navigation message demodulation using external information, e.g. extracted from GFZ's "NavBit" data base, is preferable to internal demodulation. Open-loop signal tracking results are insensitive to the receiver-internal Doppler model for carrier signal-to-noise density ratios $C/N_0 \gtrsim 30$ dB Hz; below this value reconstructed Doppler frequencies gravitate towards the model value and thus potentially constitutes a bias source.

Acknowledgements. Helpful discussions with S. Heise are gratefully acknowledged. We thank C. Selke and M. König for the design and assembly of the OpenGPS hardware and Potsdam Institute for Climate Impact Research for access to the observation deck on building A31. GPS broadcast ephemeris data were provided by GFZ's orbit processing group at Oberpfaffenhofen, Germany. The "OpenGPS" receiver software is derived from from the GPL-licensed "OpenSourceGPS" code base written by Clifford Kelley with contributions from Stephan Esterhuizen and Sam Storm van Leeuwen. Access to GFZ's NavBit data base is provided by the Information System and Data Center (ISDC) at http://isdc.gfz-potsdam.de, project: "GNSS", product type: "GNSS-GPS-1-NAVBIT". The "OpenGPS" software as well as the "GLESER" measurement data are available on request from the first author. The European Centre for Medium-Range Weather Forecasts (ECMWF) is acknowledged for access to meteorological analysis data; information on access to ECMWF data is available at http://www.ecmwf.int. Trademarks are owned by their respective owners.

References

Anthes, R. A., Bernhardt, P. A., Chen, Y., Cucurull, L., Dymond, K. F., Ector, D., Healy, S. B., Ho, S.-P., Hunt, D. C., Kuo, Y.-H., Liu, H., Manning, K., McCormick, C., Meehan, T. K., Randel, W. J., Rocken, C., Schreiner, W. S., Sokolovskiy, S. V., Syndergaard, S., Thompson, D. C., Trenberth, K. E., Wee, T.-K., Yen, N. L., and Zeng, Z.: The COSMIC/FORMOSAT-3 Mission: Early Results, Bull. Am. Meteorol. Soc., 89, 313–333, doi:10.1175/BAMS-89-3-313, 2008.

Ao, C. O., Hajj, G. A., Meehan, T. K., Dong, D., Iijima, B. A., Mannucci, A. J., and Kursinski, E. R.: Rising and setting GPS occultations by use of open-loop tracking, J. Geophys. Res., 114, D04101, doi:10.1029/2008JD010483, 2009.

Axelrad, P., Larson, K., and Jones, B.: Use of the correct satellite repeat period to characterize and reduce site-specific multipath errors, in: Proceedings of the 18th International Technical Meeting of the Satellite Division of The Institute of Navigation (ION GNSS 2005), pp. 2638–2648, IEEE, Long Beach, CA, 2005.

Badke, B.: What is C/N_0 and how is it calculated in a GNSS receiver?, InsideGNSS, 4, 20–23, 2009.

Beyerle, G., Gorbunov, M. E., and Ao, C. O.: Simulation studies of GPS radio occultation measurements, Radio Sci., 38, 1084, doi:10.1029/2002RS002800, 2003.

Beyerle, G., Wickert, J., Schmidt, T., and Reigber, C.: GPS radio occultation with GRACE: Atmospheric profiling utilizing the zero difference technique, Geophys. Res. Lett., 32, L13806, doi:10.1029/2005GL023109, 2005.

Beyerle, G., Ramatschi, M., Galas, R., Schmidt, T., Wickert, J., and Rothacher, M.: A data archive of GPS navigation messages, GPS Solutions, 13, 35–41, doi:10.1007/s10291-008-0095-y, 2009.

Beyerle, G., Grunwaldt, L., Heise, S., Köhler, W., König, R., Michalak, G., Rothacher, M., Schmidt, T., Wickert, J., Tapley, B. D., and Giesinger, B.: First results from the GPS atmosphere sounding experiment TOR aboard the TerraSAR-X satellite, Atmospheric Chemistry and Physics, 11, 6687–6699, doi:10.5194/acp-11-6687-2011, 2011.

Bonnedal, M., Christensen, J., Carlström, A., and Berg, A.: Metop-GRAS in-orbit instrument performance, GPS Solutions, 14, 109–120, doi:10.1007/s10291-009-0142-3, 2010.

Choi, K., Bilich, A., Larson, K. M., and Axelrad, P.: Modified sidereal filtering: Implications for high-rate GPS positioning, Geophysical Research Letters, 31, L22608, doi:10.1029/2004GL021621, http://dx.doi.org/10.1029/2004GL021621, l22608, 2004.

Cucurull, L., Derber, J. C., Treadon, R., and Purser, R. J.: Assimilation of Global Positioning System Radio Occultation Observations into NCEP's Global Data Assimilation System, Mon. Wea. Rev., 135, 3174–3193, doi:10.1175/MWR3461.1, 2007.

Foelsche, U., Scherllin-Pirscher, B., Ladstädter, F., Steiner, A. K., and Kirchengast, G.: Refractivity and temperature climate records from multiple radio occultation satellites consistent within 0.05%, Atmos. Meas. Tech., 4, 2007–2018, doi:10.5194/amt-4-2007-2011, 2011.

Gleisner, H. and Healy, S. B.: A simplified approach for generating GNSS radio occultation refractivity climatologies, Atmos. Meas. Tech., 6, 121–129, doi:10.5194/amt-6-121-2013, 2013.

Gorbunov, M. E.: Radio-holographic analysis of Microlab-1 radio occultation data in the lower troposphere, J. Geophys. Res., 107, 4156, doi:10.1029/2001JD000889, 2002.

Gorbunov, M. E., Benzon, H.-H., Jensen, A. S., Lohmann, M. S., and Nielsen, A. S.: Comparative analysis of radio occultation processing approaches based on Fourier integral operators, Radio Sci., 39, RS6004, doi:10.1029/2003RS002916, 2004.

Gorbunov, M. E., Vorob'ev, V. V., and Lauritsen, K. B.: Fluctuations of refractivity as a systematic error source in radio occultations, Radio Sci., 50, doi:10.1002/2014RS005639, 2015.

Haase, J. S., Murphy, B. J., Muradyan, P., Nievinski, F. G., Larson, K. M., Garrison, J. L., and Wang, K.-N.: First results from an airborne GPS radio occultation system for atmospheric profiling, Geophys. Res. Lett., 40, 1759–1765, doi:10.1002/2013GL058681, 2014.

Hajj, G. A., Ao, C. O., Iijima, B. A., Kuang, D., Kursinski, E. R., Mannucci, A. J., Meehan, T. K., Romans, L. J., de la Torre Juarez, M., and Yunck, T. P.: CHAMP and SAC-C atmospheric occultation results and intercomparisons, J. Geophys. Res., 109, D06109, doi:10.1029/2003JD003909, 2004.

Healy, S.: Abel transform inversion of radio occultation measurements made with a receiver inside the Earth's atmosphere, Ann. Geophys., 20, 1253–1256, doi:10.5194/angeo-20-1253-2002, 2002.

Healy, S. B. and Thepaut, J. N.: Assimilation experiments with CHAMP GPS radio occultation measurements, Q. J. R. Meteorol. Soc., 132, 605–623, doi:10.1256/qj.04.182, 2006.

Helm, A.: Ground-based GPS altimetry with the L1 OpenGPS receiver using carrier phase-delay observations of reflected GPS signals, Scientific technical report STR 08/10, Deutsches Geoforschungszentrum GFZ, Potsdam, Germany, doi:10.2312/GFZ.b103-08104, 2008.

Hocke, K., Pavelyev, A. G., Yakovlev, O. I., Barthes, L., and Jakowski, N.: Radio occultation data analysis by the radioholographic method, J. Atmos. Solar-Terr. Phys., 61, 1169–1177, 1999.

Kaplan, E. D.: Understanding GPS: Principles and applications, Artech House, Boston, London, 1996.

Kelley, C.: Internet-based open source software for learning about GPS, GPS Solutions, 6, 201–205, doi:10.1007/s10291-002-0026-2, 2002.

Kursinski, E. R., Hajj, G. A., Schofield, J. T., Linfield, R. P., and Hardy, K. R.: Observing Earth's atmosphere with radio occultation measurements using Global Positioning System, J. Geophys. Res., 19, 23,429–23,465, doi:10.1029/97JD01569, 1997.

Lindsey, W. C. and Chie, C. M.: A survey of digital phase-locked loops, Proceedings of the IEEE, 69, 410–431, doi:10.1109/PROC.1981.11986, 1981.

Liu, Y. and Xue, J.: Assimilation of GNSS radio occultation observations in GRAPES, Atmos. Meas. Tech., 7, 3935–3946, doi:10.5194/amt-7-3935-2014, 2014.

Lowry, A. R., Rocken, C., Sokolovskiy, S. V., and Anderson, K. D.: Vertical profiling of atmospheric refractivity from ground-based GPS, Radio Science, 37, 13–1–13–19, doi:10.1029/2000RS002565, 2002.

Luntama, J.-P., Kirchengast, G., Borsche, M., Foelsche, U., Steiner, A., Healy, S., von Engeln, A., O'Clerigh, E., and Marquardt, C.: Prospects of the EPS GRAS Mission For Operational Atmospheric Applications, Bull. Am. Meteorol. Soc., 89, 1863–1875, doi:10.1175/2008BAMS2399.1, 2008.

Misra, P. and Enge, P.: Global Positioning System: Signals, Measurements, and Performance, Ganga-Jamuna Press, Lincoln, MA 01773, USA, 2006.

Parkinson, B. W. and Spilker, J. J., eds.: Global Positioning System: Theory & Applications, Volume I&II, Am. Inst. of Aeronautics and Astronautics, Washington, DC, 1996.

Poli, P., Healy, S. B., and Dee, D. P.: Assimilation of Global Positioning System radio occultation data in the ECMWF ERA-Interim reanalysis, Q. J. R. Meteorol. Soc., 136, 1972–1990, doi:10.1002/qj.722, 2010.

Rennie, M. P.: The impact of GPS radio occultation assimilation at the Met Office, Q. J. R. Meteorol. Soc., 136, 116–131, doi:10.1002/qj.521, 2010.

Ringer, M. A. and Healy, S. B.: Monitoring twenty-first century climate using GPS radio occultation bending angles, Geophys. Res. Lett., 35, L05708, doi:10.1029/2007GL032462, 2008.

Rocken, C., Anthes, R., Exner, M., Hunt, D., Sokolovskiy, S., Ware, R., Gorbunov, M., Schreiner, W., Feng, D., Herman, B., Kuo, Y.-H., and Zou, X.: Analysis and validation of GPS/MET data in the neutral atmosphere, J. Geophys. Res., 102, 29,849–29,866, doi:10.1029/97JD02400, 1997.

Schmidt, T., Wickert, J., and Haser, A.: Variability of the upper troposphere and lower stratosphere observed with GPS radio occultation bending angles and temperatures, Advances in Space Research, 46, 150–161, doi:10.1016/j.asr.2010.01.021, 2010.

Sokolovskiy, S., Rocken, C., Hunt, D., Schreiner, W., Johnson, J., Masters, D., and Esterhuizen, S.: GPS profiling of the lower troposphere from space: Inversion and demodulation of the open-loop radio occultation signals, Geophys. Res. Lett., 33, L14816, doi:10.1029/2006GL026112, 2006.

Sokolovskiy, S., Rocken, C., Schreiner, W., Hunt, D., and Johnson, J.: Postprocessing of L1 GPS radio occultation signals recorded in open-loop mode, Radio Sci., 44, RS2002, doi:10.1029/2008RS003907, 2009.

Sokolovskiy, S., Rocken, C., Schreiner, W., and Hunt, D.: On the uncertainty of radio occultation inversions in the lower troposphere, J. Geophys. Res., 115, D22111, doi:10.1029/2010JD014058, 2010.

Sokolovskiy, S. V.: Tracking tropospheric radio occultation signals from low Earth orbit, Radio Sci., 36, 483–498, doi:10.1029/1999RS002305, 2001.

Sokolovskiy, S. V., Rocken, C., and Lowry, A. R.: Use of GPS for estimation of bending angles of radio waves at low elevations, Radio Sci., 36, 473–482, doi:10.1029/2000RS002541, 2001.

Steiner, A. K., Lackner, B. C., Ladstädter, F., Scherllin-Pirscher, B., Foelsche, U., and Kirchengast, G.: GPS radio occultation for climate monitoring and change detection, Radio Sci., 46, RS0D24, doi:10.1029/2010RS004614, 2011.

Thomas, J. B.: An analysis of digital phase-locked loops, JPL Publication 89-2, Jet Propulsion Laboratory, Pasadena, USA, 1989.

Tsui, J. B.-Y.: Fundamentals of Global Positioning System Receivers: A Software Approach, John Wiley & Sons, Inc., New York, 2000.

van Leeuwen, S.: GPS point position calculation, GPS Solutions, 6, 115–117, doi:10.1007/s10291-002-0003-9, 2002.

von Engeln, A., Andres, Y., Marquardt, C., and Sancho, F.: GRAS radio occultation on-board of Metop, Advances in Space Research, 47, 336–347, doi:10.1016/j.asr.2010.07.028, 2011.

Wickert, J., Reigber, C., Beyerle, G., König, R., Marquardt, C., Schmidt, T., Grunwaldt, L., Galas, R., Meehan, T. K., Melbourne, W. G., and Hocke, K.: Atmosphere sounding by GPS radio occultation: First results from CHAMP, Geophys. Res. Lett., 28, 3263–3266, doi:10.1029/2001GL013117, 2001.

Wickert, J., Beyerle, G., König, R., Grunwaldt, L., Heise, S., Michalak, G., Reigber, C., and Schmidt, T.: GPS radio occultation with CHAMP and GRACE: A first look at a new and promising satellite configuration for global atmospheric sounding, Ann. Geophys., 23, 653–658, 2005.

Zarlink: GP2021 GPS 12-channel correlator, Zarlink Semiconductor Inc., 2005.

Zuffada, C., Hajj, G. A., and Kursinski, E. R.: A novel approach to atmospheric profiling with a mountain-based or airborne GPS receiver, J. Geophys. Res., 104, 24,435–24,448, doi:10.1029/1999JD900766, 1999.

Zus, F., Beyerle, G., Heise, S., Schmidt, T., Wickert, J., and Marquardt, C.: Validation of refractivity profiles derived from GRAS raw-sampling data, Atmospheric Measurement Techniques, 4, 1541–1550, doi:10.5194/amt-4-1541-2011, 2011.

Zus, F., Grunwaldt, L., Heise, S., Michalak, G., Schmidt, T., and Wickert, J.: Atmosphere sounding by GPS radio occultation: First results from TanDEM-X and comparison with TerraSAR-X, Adv. Space Res., 53, 272–279, doi:10.1016/j.asr.2013.11.013, 2014.

Zus, F., Dick, G., Heise, S., and Wickert, J.: A forward operator and its adjoint for GPS slant total delays, Radio Sci., 50, 393–405, doi:10.1002/2014RS005584, 2015.